Zhang, B., Lei, J., Yuan, X., Zhang, G., He, J., Xu, Q. (2020): Detailed Moho variations under Northeast China inferred from receiver function analyses and their tectonic implications. - Physics of the Earth and Planetary Interiors, 300, 106448.

https://doi.org/10.1016/j.pepi.2020.106448

Detailed Moho variations under Northeast China inferred from receiver function analyses and their tectonic implications

Bing Zhang[1,2], Jianshe Lei[2*], Xiaohui Yuan[3], Guangwei Zhang[2], Jing He[2], Qiang Xu[4]

[1] Institute of Geophysics, China Earthquake Administration, Beijing 100081, China

[2] Key Laboratory of Crustal Dynamics, Institute of Crustal Dynamics, China Earthquake Administration, Beijing 100085, China

[3] Deutsches GeoForschungsZentrum GFZ, Telegrafenberg, Potsdam 14473, Germany

[4] Institute of Tibetan Plateau Research, China Academy of Sciences, Beijing 100101, China

*Corresponding author: J. Lei

E-mail: jshlei_cj@126.com

Abstract In this study we investigate detailed Moho variations beneath Northeast China by applying the arithmetic mean, back-projected and Fresnel-zone migration imaging methods to a total of 169,602 high-quality P-wave receiver functions from seismograms of 2903 teleseismic events recorded at 127 NECESSArray stations and 321 China Earthquake Administration stations. Our results show that the Moho depth variations are correlated with the surface geology in the study region. The Moho is deeper (~34.0-42.0 km) under the Great Xing'an range, the Lesser Xing'an range, the Zhangguangcai range, and the Changbaishan mountain, whereas it is shallower (~26.0-32.0 km) under the Songliao basin. Our results also reveal obvious Moho variations across the North-South Gravity Lineament. The Moho offsets up to ~5.0 km are clearly observed under the Nenjiang-Balihan, Yilan-Yitong, and Dunhua-Mishan faults, indicating that they are lithospheric-scale faults. A deeper Moho is revealed under the volcanoes, such as the Jingpohu, Wudalianchi, and Changbaishan volcanoes and Abaga and Halaha volcanic groups. In particular, the Moho under the Changbaishan volcano reaches ~40.0 km depth and the observation varies with the teleseismic back-azimuths, suggesting a complicated magma system in the crust. In addition, the Moho under the Songliao basin varies significantly from ~26.0 km depth in the east to ~32.0 km depth in the west, which could be related to the lithosphere extension and thinning. All these results suggest that there exists to a hot and wet

mantle upwelling in the big mantle wedge formed by the deep dehydration of the long stagnant Pacific slab in the mantle transition zone under Northeast China.

Keywords: Receiver function; Migration imaging; Moho depth; Northeast China

1. Introduction

Northeast China (NE China), located in the eastern segment of the Central Asian Orogenic Belt, is bounded by the Siberian Craton to the north, the North China Craton to the south, and the Japan Sea to the east (Ren et al., 2002). The study region is composed of several tectonic blocks due to serial episodes of continental accretions since the Paleozoic, including the Great Xing'an range in the west, the Songliao basin in the center, the Lesser Xing'an range in the north, the Changbaishan mountain and the Zhuangguangcai range in the east, and the Yanshan orogenic belt in the south (Fig. 1).

The west-east closure of the Mongol-Okhotsk ocean occurred along the Mongol-Okhotsk suture in the late Jurassic, and the Paleo-Asian ocean progressively closed along the Solonker suture in the late Permian or early Triassic (e.g., Wu et al., 2004, 2007; Xu et al., 2009; Meng et al., 2010, 2011; Xu et al., 2013; Tang et al., 2014). Since the late Jurassic and Cretaceous, NE China has been undergoing large-scale crustal extension and extensive volcanism since the collision of the Okhotsk ocean (e.g., Sengör et al., 1993; Meng, 2003; Ren et al., 2002) and the westward subduction of the Pacific plate (e.g., Zhao, 2004; Lei and Zhao, 2005, 2006; Huang and Zhao, 2006; Wei et al., 2012; Chen et al., 2017; Lei et al., 2018; Ma et al., 2018). The crustal extension has probably resulted in the formation of a series of intra-continental basins, including the Songliao basin, the Erlian basin and the Hailar basin. Furthermore, around the Songliao basin a series of volcanoes have been formed, such as the Wudalianchi volcano to the north and Shuangliao volcano to the south. To the east, the Changbaishan volcano, the Longgang volcano and the Jingpohu volcano are located on the Changbaishan mountain, whereas, to the west, the Nuominhe, Halaha, and Abaga volcanic groups are laid on the Great Xing'an range. In addition, there are the North-South Gravity Lineament, the Nenjiang-Balihan fault, the Yilan-Yitong fault, and the Dunhua-Mishan fault in NE China (Fig. 1). These abundant geological phenomena have being attracted many geoscientists to conduct a series of geophysical (e.g., Lei and Zhao, 2005, 2006; Chen et al., 2011; Pan et al., 2014; Huang and Zhao, 2006; Wei et al., 2012; Zhao and Tian, 2013; Tao et al., 2014; Tang et al., 2014; Guo et al., 2016, 2018; Tian et al., 2016; Chen et al., 2017; Lei et al., 2013, 2018; Ma et al., 2018; Du and Lei, 2019; Lu et al., 2019; Yang et al., 2019a, 2019b; Zhang et al., 2019a, 2019b), geological (e.g., Xu et al., 2009, 2013; Meng et al., 2010, 2011), and petrological and geochemical studies (e.g., Liu, 1999, 2000; Fan and Hooper, 1991; Fan et al., 2001, 2011, 2012). These investigations have placed constraints on the deep origin of volcanism and mantle dynamics in NE China.

The crust-mantle boundary, known as the Moho, is one of the most important discontinuities in the Earth's interior, and it can provide key constraints on the crust and upper mantle geodynamic evolutional processes of NE China. Although a variety of geophysical methods are applied to investigate the Moho discontinuity in the study region, such as Bouguer gravity anomaly inversions (e.g., Guo et al., 2012), Pn tomography (e.g., Liang et al., 2004; Du and Lei, 2019; Yin et al., 2019), surface-wave tomography (e.g., Huang et al., 2014), and seismic explosion experiments (e.g., Zhang et al., 2002; Lu and Xia, 1993; Yang et al., 1996; Li et al., 2006), the receiver function approach is regarded as one of the most efficient tools in mapping the Moho discontinuity in an area wherever the seismic stations are available. To date, there are several receiver function studies in the study area (e.g., Zhang et al., 2013; Zhang et al., 2014; Tao et al., 2014; He et al., 2014). However, these studies focused on their own interested scientific issues in specific areas. For example, Zhang et al. (2013) applied the common-conversion-point (CCP) and H-κ stacking methods to the P-wave receiver functions recorded at two dense linear seismic arrays across the Songliao basin and at the China Earthquake Administration (CEA) stations (Zheng et al., 2010) in NE China from June 2009 to August 2011. Zhang et al. (2014) applied the CCP stacking method to the S-wave receiver functions recorded at one of the two dense linear arrays across the Songliao basin used by Zhang et al. (2013). Tao et al.

(2014) applied the H-β grid searching method to P-wave receiver functions recorded at the NECESSArray stations (e.g., Guo et al., 2014) from September 2009 to August 2011 and at the CEA stations from July 2007 to July 2010. He et al. (2014) applied the H-κ grid searching technique to P-wave receiver functions recorded at the two dense linear arrays as used by Zhang et al. (2013) and at CEA stations from 2009 to 2010. All these results illustrated a similar pattern of the Moho variations in the study region, that is, a shallower Moho discontinuity under the Songliao basin and a deeper Moho discontinuity under the Great Xiang'an range and Changbaishan mountain (e.g., Zhang et al., 2013, 2014; Tao et al., 2014; He et al., 2014). However, detailed Moho variations under the volcanoes and across the faults are still unresolved. These variations are important for understanding the mantle dynamics of NE China.

In this study, we collect as many as possible high-quality receiver functions from the densely distributed stations in NE China, including 321 CEA stations from January 2008 to October 2016 and 127 NECESSArray stations from September 2009 to August 2011 (Fig. 1). These unprecedented data allow us to construct a high-resolution Moho depth map for the region. Furthermore, three kinds of receiver function imaging techniques, the arithmetic mean, back-projected and Fresnel-zone migration imaging techniques, are adopted to better constrain the absolute depth of the Moho and provide detailed Moho lateral variations under the volcanoes and across the faults. Our present model with more detailed crustal structure provides new insights into the mantle dynamics of NE China.

2. Data and method

In this study, we collect seismogram from a total of 448 stations (Fig. 1). The 127 NECESSArray stations (white triangles in Fig. 1; Guo et al., 2014) were deployed from September 2009 to August 2011, whereas the data from the 321 CEA stations (blue triangles in Fig. 1; Zheng et al., 2010) were collected during January 2008 to October 2016. The station spacing is less than 70 km in most of the study area. In order to obtain sufficient high-quality receiver functions, two different data selection criteria are adopted for different network stations. For the CEA stations with a long operation time, we set the event magnitudes to great than 5.5 and obtain a total number of 2220 teleseismic events. For the NECESSArray stations, due to their shorter operation time, we set the minimal magnitude to greater than 5.0 and obtain 683 events for receiver functions. All these events (Fig. 2) are distributed from 30^o to 95^o in epicenter distance, and they have good azimuthal coverage around the study region. Such a data set allows us to obtain the detailed Moho variations in the study region.

The P-wave receiver function computation is performed by following the procedures described in detail by Yuan et al. (1997). For each station, all the seismograms are cut using a time window of 10 s prior to and 100 s after the theoretical direct P arrival times. The instrument responses, linear trends and mean values of the raw data are removed. The traces with clear P-wave onsets are manually selected and high signal-to-noise ratios (larger than 5.0) have been visually inspected for the calculation of P receiver functions. The Z, NS and EW (ZNE) components in the Cartesian coordinate system are rotated into local P-SV-SH (LQT) components in the ray coordinate system based on the event back-azimuths and incidence angles. The P-wave receiver functions are obtained by deconvolving the P from the SV components. Finally, a total number of 169,602 receiver functions are visually selected. In order to eliminate the effects of Ps arrival time differences due to epicentral distances and focal depths, the moveout correction is performed with a reference slowness of 6.4 s/deg.

Following the procedures mentioned above, we calculate the receiver functions in the present study. We carefully determine some major parameters, such as frequencies and bin sizes, to achieve the most optimal performance of migration with this data set. Considering that the receiver functions contain the amplitudes and delay times of the direct Pms converted phase and multiples of discontinuities at different depths, three kinds of receiver function stacking techniques have been used along the cross sections to enhance the imaging robustness. These techniques are (1) the arithmetic mean of all the receiver functions at each station (e.g., Kind et al., 2002; Yuan et al., 1997; Gilligan et al., 2015), (2) the back-projected migration or CCP stacking (Kosarev et al., 1999), (3) the Fresnel-zone projection migration (e.g., Kind et al., 2002; He et al., 2018). For the first kind of stack imaging, in order to compare receiver functions with different filter bands, all the receiver function traces are filtered within three frequency bands, 0.02-0.5 Hz, 0.02-1.0 Hz, and 0.02-2.5 Hz. It is visible from Figs. 3 and 4 that the higher the filter frequency is, the more detailed structure the receiver function waveforms show. However, the receiver functions at the high and intermediate frequency bands of 0.02-1.0 Hz, and 0.02-2.5 Hz show two small positive peaks, whereas those at the lower pass frequency band of 0.02-0.5 Hz display one large peak (Figs. 3 and 4). Therefore, to reliably identify the Moho discontinuity, we choose a lower pass frequency band of 0.02-0.5 Hz in the following migration imaging. Over 500 high-quality receiver function traces are manually collected for each CEA station, and around 150 receiver function traces are obtained for most NECESSArray stations. The ample number of recordings make excellent back-azimuthal coverage around each station. Applying the back-projection migration techniques, all the amplitudes per bin are back-projected along ray paths, stacked and normalized by the number of the traces hitting the same bin, whereas the amplitude values of bins with no rays are assigned to be zero. The cell is set to 1 km in both horizontal and vertical directions. One more imaging technique we performed is the Fresnel-zone projection migration. As the width of the Fresnel zone represents the minimal lateral resolution of the CCP stacking and it varies with depth (Kind et al., 2002), we define the size of the first Fresnel zone as the horizontal smoothing factor to generate the final image. The 1-D layered IASP91 velocity model (Kennett and Engdahl, 1991) and a Vp/Vs ratio of 1.73 are used in the latter two migration imagings. For the latter two kinds of migration techniques, eleven profiles P1-P11 are illustrated (Figs. 5-7), including five east-west profiles (P1-P5) passing through the Great Xing'an range, Songliao basin, and Zhangguangcai range and nearly perpendicular to the faults and the North-South Gravity Lineament, three north-south profiles (P6-P8) along the strike of the Great Xing'an range and across the Songliao basin from the south to the north, and three profiles (P9-P11) passing through the Changbaishan, Jingpohu and Longgang volcanoes. Moreover, we illustrate the 2D overall architecture of the Moho variations to reveal the lateral variation of crust thickness in the study region (Fig. 8a). Detailed procedures for obtaining our present Moho discontinuity are introduced in Fig. S1 in the Appendix A.

Some tests by Kind et al. (2002) and Caldwell et al. (2013) suggested that the Moho depth uncertainties are less than 3 km if a change amounts to 5% in the crustal P wave velocity or Vp/Vs ratio. Meanwhile, the computation errors could also be caused by reading errors of Pms and PpPs in Figs. 3, 4, and 6. According to the previous study by Yuan et al. (2002), the errors of measured Moho depth results in Figs. 7 and 8a can amount to ~1.5 km due to the reading uncertainties of ~0.5 s. Such Moho errors could not significantly affect the identification of the main structural features appeared in our present study.

3. Results

3.1 Receiver function analysis beneath the stations

Fig. 3 shows examples for individual receiver functions at three filter bands of 0.02-0.5 Hz, 0.02-1.0 Hz, and 0.02-2.5 Hz recorded at eight stations in different tectonic units. Fig. 4 illustrates the stacked receiver functions in each back-azimuthal bin with a size of 10^{o} for the stations to enhance the signal-to-noise ratio. A prominent maximal positive amplitude marked by red bulges from ~3.5 to ~6 s are clearly identified in the summation traces for all the stations (Figs. 3 and 4), which represents the Pms conversion energy caused by the Moho discontinuity. For stations CHR and NE52 located in the Great Xing'an range (Fig. 5), there is a distinct positive phase after 5.0 s, but most receiver function waveforms at station NE52 are much more disorder than station CHR (Figs. 3 and 4), which indicates a more complicated crustal structure beneath the southern Great Xing'an range than its northern part. Station NE58 in the eastern Songliao basin (Fig. 5) shows that positive Ps conversion at 4.0 s is dominant in most of the receiver functions (Figs. 3 and 4). Compared to the eastern basin, station NE78 situated in the western Songliao basin (Fig. 5) shows much more complicated receiver functions and a significant negative signal between 2.0 s and 4.0 s is visible (Figs. 3 and 4), which could be interpreted as the Ps conversion of the thick sedimentary layer in the region. The Pms conversion with relatively weaker energy beneath station MJT in the Zhangguangcai range (Fig. 5) appears about 0.5 s later than those stations in the basin (Figs. 3 and 4), implying a reduction of Moho depth of several kilometers from the Zhangguangcai range to the Songliao basin. For station CBS on the Changbaishan volcano (Fig. 5), the arrival times of Moho phase in the individual traces show distinct back-azimuthal variations (Figs. 3 and 4). Furthermore, a significant negative signal emerges at about 2.0 s in the back-azimuth of 180°-230° (Figs. 3 and 4). At stations WDL and DAX very close to the Wudalianchi volcano and the Datong volcano (Fig. 5), a positive Pms conversion lags behind 4.0 s, but a Pms conversion doublet can be clearly observed at 5.0 s beneath station DAX in the North China Craton (Figs. 3 and 4).

Receiver functions from different back-azimuths at station CBS, 4 km north to the Tianchi crater, are displayed in our images (Figs. 3 and 4). The Pms arrival times change with back-azimuths, being earlier from the south than from the north. Despite the Pms phase, in the east (back-azimuth ~0°-160°) there is one more similar clear phase with positive energy at ~3 s, suggesting the existence of one more shallow-seated velocity discontinuity beneath the station. However, to the southwest (back-azimuth ~180°-270°), a dominant negative phase is observed at ~3 s, indicating a low-velocity layer in the mid-lower crust.

3.2 Stacked receiver functions along the profiles

Fig. 6 shows images of binning stacked receiver functions along different profiles as shown in Fig. 5. Along profiles P1-P5, the Pms phases generally appear later by up to ~2 s in the west than in the east (Fig. 6a-e), which is equivalent to a Moho deepening of ~16 km. The amplitude of Pms within ~120°E to ~130°E significantly amplifies possibly due to the thick sedimentary layer beneath the Songliao basin (Fig. 6c-d). As shown in Fig. 6f-h, an evident strengthening of the Pms phase energy beneath the basins can be distinguished along three north-south profiles P6-P8, which is consistent with the thick sedimentary under the subsurface. Specifically, a small delay in the Pms arrival is observed from the north Yanshan orogenic belt to the Erlian basin along profile P6 (Fig. 6f). As shown in Fig. 6g-h, profiles P7 and P8 show that Pms conversions appear a little later in the northern Songliao basin than in its southern part, suggesting that the Moho discontinuity deepens slightly in the south-north direction. Along profiles P9-P11, it is remarkable that the delay times of Pms conversions differ by up to ~1 s between the Changbaishan volcano and the Jingpohu and Longgang volcanoes (Fig. 6i-k).

3.3 Back-projected and Fresnel-zone migrations

Fig. 7 illustrates the Moho discontinuity along eleven profiles imaged by both back-projected and the Fresnel-zone migration imaging techniques. It is visible that the Moho discontinuity imaged by both techniques shows a strong positive signal with a very consistent variation with the surface tectonics. In the study region, the Moho discontinuity can be coherently identified at depths of ~26.0-45.0 km (Fig. 7).

Along profile P1, a gently shallow Moho discontinuity is observed from ~45.0 km depth under the Yanshan orogenic belt to ~30.0 km depth under the Bohai Bay basin (Fig. 7a), whereas the Moho varies relatively rapidly from ~42.0 km depth under the Great Xing'an range to ~28.0 km depth under the Songliao basin (Fig. 7b). However, the other three east-west profiles (P3-P5) show a much more complicated Moho discontinuity with more localized and undulated variations, including an eastward thinning from ~40.0 km depth under the Great Xing'an Range to ~32.0 km depth under the Songliao basin further to ~38.0 km depth under the Zhangguangcai range. Note that the Moho discontinuity shows an abrupt change of ~5.0 km across the Nenjiang-Balihan fault and Yilan-Yitong fault (Fig. 7c-e). West of the North-South Gravity Lineament, the Moho discontinuity shows a general varying trend from ~ 45.0 km depth under the northern Yanshan orogenic belt to ~35.0 km depth under the Erlian basin (Fig. 7f), whereas to the east it is nearly flat (~32.0-35.0 km depth) in the western Songliao basin (Fig. 7g). The central Songliao basin is characterized by a much more detailed crustal feature from the south to the north (Fig. 7h). Meanwhile, the Changbaishan volcano shows a much deeper Moho discontinuity (~42.0 km depth) than the Jingpohu and Longgang volcanoes (~36.0 km) (Fig. 7i-k).

3.4 Variations of the crustal thickness

Fig. 8a illustrates the measured crustal thickness in map view. The detailed procedures for obtaining the Moho discontinuity in the present study are described in

Fig. S1 in the Appendix A, and the corresponding Moho depth values are listed in Table S1 in the Appendix B. It is visible that our results show significant lateral variations from ~26.0 to ~45.0 km depth in the study region, and such variations are closely correlated with the surface geological features. In general, the Moho varies distinctly from west to east, from ~42.0 km depth under the Great Xing'an range in the west, to ~28.0 km depth under the Songliao basin in the center, and ~38.0 km depth under the Zhangguangcai range in the east. Furthermore, some small basins, such as the Erlian basin, Hailar basin and Sanjiang basin, show a relatively shallower Moho discontinuity, and across the North-South Gravity Lineament and the Nenjiang-Balihan and Yilan-Yitong faults there are sharp variations in the Moho discontinuity. Under the Changbaishan, Jingpohu, Wudalianchi, and Shuangliao volcanoes and the Abaga and Halaha volcanic groups, the Moho is deeper than the surrounding areas, suggesting the existence of magmatism in the crust and upper mantle.

4. Discussion

4.1 Comparison with previous Moho studies in NE China

Several researchers have studied the Moho using the receiver function analysis in NE China (e.g., Zhang et al., 2013; Zhang et al., 2014; Tao et al., 2014) or in the entire China including NE China (e.g., He et al., 2014; Li et al., 2014). Generally, there is a similar pattern between our present (Figs. 7 and 8) and previous results. A relatively deeper Moho is revealed under the Great Xing'an rang and Zhangguangcai rang, whereas a shallower one is observed under the Songliao basin. Furthermore, a deeper Moho has imaged under the Changbaishan and Wudalianchi volcanoes and Abaga volcanic group. However, there are some differences between our present (Figs. 7 and 8) and previous studies. For example, our results clearly reveal a sharper variation of the Moho discontinuity cross the Great Xing'an range, the Nenjiang-Balihan and Yilan-Yitong faults in NE China, and a much deeper Moho under the Changbaishan volcano (Figs. 7 and 8) than previous results (e.g., Tao et al., 2014). Such differences could be due to a much large data set with good coverage of receiver functions used in the present study (Figs. 1 and 2). Furthermore, in the present study, high-quality receiver functions have been visually inspected and carefully selected with consideration of high signal-to-noise ratio and degree of consistency when receiver functions are grouped in back-azimuthal and epicentral distance at the same station. Last but not least, calculation procedures of receiver functions adopted in this study are different from those in the previous studies (Liu and Niu, 2011; Tao et al., 2014). Liu and Niu (2011) and Tao et al. (2014) rotated the seismograms from ZNE to ZRT system, whereas we further make a rotation from ZRT to LQT system based on the incidence angles in the present study. An important advantages of the LQT system is that the energy of the direct P wave disappears in the Q component, so that the Q component receiver functions can precisely distinguish Ps conversions from shallow interfaces. Therefore, we can conclude that our results are more robust than previous studies.

4.2 Moho discontinuity across the ranges

The major orogenic belts in NE China contain the Great Xing'an range in the west, the Lesser Xing'an range in the north, and the Zhangguangcai range and the Changbaishan mountain in the east. A marked difference of the Moho discontinuity is clearly imaged in our study (Figs. 7 and 8). The deepest Moho is ~42.0 km under the Great Xing'an range. The Moho shallows to ~38.0 km under the Zhangguangcai range and to ~34.0 km under the Lesser Xing'an range (Figs. 7 and 8). The Moho depth variation is in agreement with previous receiver function analyses (e.g., Wei and Chen, 2012; Zhang et al., 2013, 2014; He et al., 2014; Li et al., 2014; Tao et al., 2014), active source explosion experiments (e.g., Li et al., 2006; Lu and Xia, 1993), and gravity, magnetic, and electrical studies (e.g., Hao et al., 1997; He et al., 2014). In addition, geochemical studies showed that the granitic crystalline basements in different areas of NE China were formed at different ages (e.g., Zhang et al., 2010; Meng et al., 2010). The granites beneath the Great Xing'an range were mainly formed in the early Cretaceous, whereas those in the Zhangguangcai range were mainly formed in the Jurassic, suggesting that the crust of these two regions has experienced totally different tectonic evolution processes since the Mesozoic. In addition, our results also display that the Great Xing'an range has a gentle variation in the Moho discontinuity, whereas the Zhangguangcai range shows a much more complicated feature (Figs. 7 and 8). This feature is supported by Tao et al. (2014) but our results show much more clear patterns (Figs. 7 and 8) due to much more data used in the present study (Figs. 1, 2 and 6). Geological surveys further demonstrated that the Great Xing'an range is mainly composed of the ancient pediocratic Ergun block and Xing'an block, whereas the Zhangguangcai range has undergone a mosaic of several micro-continental terranes, such as the Songnen, Jiamusi, Laoyeling, Xingkai, Breya and other ancient blocks, laying the foundation for a more complicated crust structure (e.g., Zhang et al., 2006). All these results are consistent with crustal extension, lithosphere thinning and active volcanism in NE China (e.g., Tatsumi et al., 1990; Davis et al., 2004; Ren et al., 2002; Tao et al., 2014; Zhang et al., 2014), which could be associated with the big mantle wedge (BMW) structure formed by the westward deep subduction, long stagnancy and deep dehydration of the Pacific slab in the mantle transition zone (MTZ) (e.g., Zhao, 2004; Lei and Zhao, 2005, 2006; Huang and Zhao, 2006; Zhao et al., 2007, 2009; Wei et al., 2012, 2015; Zhao and Tian, 2013; Lei et al., 2018, 2020; Ma et al., 2018). A similar BMW structure has been found under eastern Tibet (e.g., Lei et al., 2019). Some low-velocity anomalies are imaged in the upper mantle under eastern Tibet, whereas high-velocity anomalies representing the subducting Indian slab are observed under the Burma arc from the upper mantle to the MTZ. Furthermore, these high-velocity anomalies under eastern Tibet in the MTZ have extended northward to the Kunlun fault zone and eastward to the Xiaojiang fault zone, which forms a long stagnant Indian slab in the MTZ (e.g., Lei et al., 2009, 2019; Lei and Zhao, 2016).

4.3 Moho discontinuity under the Songliao basin

The crustal thickness of NE China as a whole has a visible deepening trend from the Songliao basin to the peripheral orogenic belts (Figs. 7 and 8), suggesting that the Moho undulations correlate with the surface geology. Furthermore, the lithospheric-asthenospheric boundary (LAB) in NE China displays a similar structural feature, the shallowest LAB is ~70-100 km depth under the Songliao basin, the deepest LAB is ~100-160 km depth under the Great Xing'an range, and ~90-140 km under the Zhangguangcai range (e.g., Guo et al., 2014). Previous S wave receiver function analyses showed a similar variation in the LAB depth (e.g., Zhang et al., 2014). In addition, our results show that the crust under the Songliao basin thins to the east (Figs. 7b-d, 8, 9), which is different from Zhang et al. (2014) illustrating a downward bending Moho discontinuity in the central of the basin but is well consistent with other studies (e.g., Tao et al., 2014). This is also supported by geothermal studies showing that thermal activity in the eastern part of the basin is stronger than that in the west (e.g., Yang et al., 2001). Such a variation of the Moho discontinuity under the Songliao basin could be associated with the volcanism in the Zhangguancai range and Changbaishan mountain where a hot and wet mantle upwelling exits (e.g., Lei and Zhao, 2005, 2006; Duan et al., 2005, 2009; Zhao et al., 2007, 2009; Zhao and Tian, 2013).

4.4 Moho discontinuity under the volcanoes in NE China

There are many Cenozoic volcanoes in NE China, including the Changbaishan, Longgang, Jingpohu, Shuangliao, and Wudalianchi volcanoes and Abaga, Halaha, and Nuominhe volcanic groups (Figs. 1, 7, 8). In this study, due to the high density distribution of seismic stations around the volcanoes, in particular around the Changbaishan volcano, we have obtained much detailed Moho structures under these volcanoes. Our results show that the Moho discontinuities under all these volcanoes are much deeper than those under the surrounding areas (Figs. 7i-k, 8, 9). Furthermore, the Moho is ~ 40 km under the Changbaishan volcano and ~37 km under the Jingpohu volcano, which is deeper than ~34 km in the surrounding areas (Figs. 7i-k, 8, 9). The Moho discontinuity under the Longgang volcano is 4 km shallower than under the Changbaishan and Jingpohu volcanoes, which is basically concordant with the previous studies (e.g., Hetland et al., 2004; Liu and Niu, 2011). Magnetotelluric soundings showed that there is a low-resistivity body in the crust under the Changbaishan volcano (e.g., Tang et al., 1997; Qiu et al., 2014), and active source explosions illustrated low-velocity anomalies in the crust under the volcano (e.g., Zhang et al., 2002). Some previous receiver function analyses revealed higher Vp/Vs ratios under the Changbaishan volcano (e.g., Tao et al., 2014; Zhu et al., 2017), which are interpreted as the existence of the mantle ferromagnesic materials in the crust, because these materials have a high temperature that could lead to partial melting or fluids in the crust (O'Connell and Budiansky, 1974; Mavko, 1980). All these results suggest the existence of magma chamber under the volcano.

Teleseismic tomographic models clearly showed columnar low-velocity anomalies under the Changbaishan volcano in the upper mantle (e.g., Lei and Zhao, 2005; Duan et al., 2009; Zhao et al., 2009). Global and regional tomograhic models revealed a long and stagnant Pacific slab in the MTZ under NE China (e.g., Zhao, 2004; Lei and Zhao, 2006; Huang and Zhao, 2006; Wei et al., 2012, 2015; Chen et al., 2017; Ma et al., 2018). Receiver function analyses illustrated a thickened MTZ under the Changbaishan volcano (e.g., Ai et al., 2003; Li and Yuan, 2003; Tian et al., 2016). Experimemtal petrology and other studies demonstrated that hydrous Mg-Si minerals in the subducted slab may continue dehydration reactions in the MTZ (e.g., Thompson, 1992; Staudigel and King, 1992), because they may not completely finish at the shallow depth (~100-200 km) of the upper mantle. Mineral physics experiments revealed that there are several times more water in the MTZ than in the other portions of the mantle, suggesting that the MTZ is an important reservoir in the Earth's interior (e.g., Inoue et al., 2004). All these results indicate that the crustal magma chamber could be fed by the hot and wet mantle upwelling in the BMW formed by the deep dehydration of the long stagnant Pacific slab in the MTZ (e.g., Zhao, 2004; Lei and Zhao, 2005, 2006; Duan et al., 2009; Huang and Zhao, 2006; Zhao et al., 2007, 2009; Wei et al., 2012, 2015; Chen et al., 2017; Lei et al., 2018, 2020; Ma et al., 2018). In view of the facts mentioned above, we propose that the abundant hot and wet ferromagnesic materials from the mantle could result in a deeper Moho discontinuity under the Changbaishan volcano.

4.5 Moho discontinuity across the faults in NE China

There are three large faults in NE China, such as the Nenjiang-Balihan fault, the Yilan-Yitong fault, and Dunhua-Mishan fault (Fig. 1). The Nenjiang-Balihan fault, known as a large NNE-SSW striking and eastward dipping normal fault, is regarded as the boundary between the Great Xing'an rang and the Songliao basin (e.g., Su et al., 2013; Xiong et al., 2016). Our results clearly reveal a rapid change up to ~5 km of the Moho discontinuity across the Nenjiang-Balihan fault (Figs. 7b-e, 8, 9), suggesting that it is a lithospheric-scale fault. The abrupt change in the Moho discontinuity is consistent with the results from the deep seismic reflection experiment by Xiong et al. (2016). On account of the activities of the Nenjiang-Balihan fault from the Cretaceous to the Cenozoic, some researchers have carried out many investigations using various approaches. Their results demonstrated obvious differences across the Nenjiang-Balihan fault in the geophysics, geomorphology and stratigraphy, confirming that the fault is a deep and large fault (e.g., Yang et al., 1996; Zhang et al., 2013). Similarly, across the Yilan-Yitong fault and Dunhua-Mishan fault, our results also show local Moho offsets near 128^{o}E and 130^{o}E (Fig. 7c-d), which is consistent with the results by Guo et al. (2012).

4.6 Mantle dynamics

Fig. 9 is an interpretation cartoon illustrating possible causes for the Moho variations in NE China. The deeper Moho discontinuities are imaged under the Great Xing'an range and Zhangguangcai range, where the shallower one is observed under the Songliao basin. The Zhangguangcai range shows a much complicated Moho discontinuity (Figs. 7-9). Across the North-South Gravity Lineament, the Nenjiang-Balihan fault, the Yilan-Yitong fault, and the Dunhua-Mishan fault, there are obvious Moho offsets (Figs. 7-9). Under the volcanoes, the Moho is deeper than the surrounding areas (Figs. 7-9). The LAB displays a significant variation from the west to the east in the study region (Fig. 9; An and Shi, 2006). All these results could be related to a hot and wet mantle upwelling in the BMW due to the deep dehydration of the subducted Pacific slab in the MTZ (Fig. 9).

5 Conclusions

In this study, we apply the arithmetic mean, back-projected, and Fresnel-zone migration imaging methods to an unprecedented amount of high-quality receiver functions collected from the CEA and NECESSArray stations in NE China. Our high-resolution Moho map reveals a significant lateral variation closely related to the surface geological features in the study region. Our results do not only display some general features revealed by the previous studies but also show some new findings.

A deeper Moho discontinuity (~34.0-45.0 km) is found under the Great Xing'an range, the Zhangguangcai range, the Lesser Xing'an range, and the Yanshan orogenic belt, whereas a shallower Moho discontinuity (~26.0-32.0 km) is observed under the Songliao basin. The Moho offsets of up to ~5.0 km are observed across the North-South Gravity Lineament, the Nenjiang-Balihan, Yilan-Yitong and Dunhua-Mishan faults, suggesting that these tectonic features are lithospheric-scale lineament and faults. Deeper Moho discontinuities are revealed under the volcanoes in NE China. Furthermore, under the Changbaishan volcano the Moho discontinuity is at ~40 km depth, and the converted phase varies around the volcano with the back-azimuths of teleseismic receiver functions, indicating that a complicated magma system may exist in the crust. All these results could be associated with a hot and wet mantle upwelling in the BMW formed by the deep dehydration of the subducted Pacific slab in the MTZ.

Acknowledgements

This work was partially supported by the National Natural Science Foundation of China (NSFC) (41530212 and 41674091) and the National Key R&D program of China (Grant nos. 2016YFC0600408 and 2018YFC1504103). The seismic waveform data recorded by the China Earthquake Administration (CEA) stations used in this study were provided by the Data Management Centre of the China National Seismic Network at the Institute of Geophysics (doi:10.11998/SeisDmc/SN) (Zheng et al., 2010), CEA, and the Heilongjiang, Jilin, Liaoning, and Neimenggu Earthquake Administrations, and those from the NECESSArray portable stations can be downloaded from the IRIS website (www.iris.edu). The GMT software package distributed by Wessel and Smith (1995) is used for making the figures. Professor Vernon Cormier (the Editor) and two anonymous referees provided thoughtful comments and suggestions that have improved this paper.

Appendix A: Procedures for obtaining the Moho discontinuity in NE China.

Appendix B: The Moho depth values obtained by our present study.

References

Ai., Y., Zheng, T., Xu, W., He, Y., Dong, D., 2003. A complex 660 km discontinuity beneath northeast China. Earth Planet. Sci. Lett. 212, 63-71.

An, M., Shi, Y., 2006. Lithospheric thickness of the Chinese continent. Phys. Earth Planet. Inter. 159, 257-266.

Caldwell, W., Klemperer, S., Lawrence, J., Rai, S., Ashish, 2013. Characterizing the Main Himalayan Thrust in the Garhwal Himalaya, India with receiver function CCP stacking. Earth Planet. Sci. Lett. 367, 15-27.

Chen, C., Zhao, D., Tian, Y., Wu, S., Hasegawa, A., Lei, J., Park, J., Kang, L., 2017. Mantle transition zone, stagnant slab and intraplate volcanism. Geophys. J. Int. 209, 68-85.

Chen, Y., Liu, Y., Huang, Z., Sun, L., 2011. Preliminary study of lateral variation in crustal structure of Northeast China from teleseismic receiver functions. Earthq. Sci. 24, 15–25.

Davis, G., Xu, B., Zheng, Y., Zhang, W., 2004. Indosinian extension in the Solonker suture zone: the Sonid Zuoqi metamorphic core complex, Inner Mongolia, China. Earth Sci. Front. 11(3), 135-144.

Deng, Q., Zhang P., Ran R., et al., 2002. Basic characteristics of active tectonics of China. Sci. China Earth Sci. 32(12), 1020–1030.

Du, M., Lei, J., 2019. Pn anisotropic tomography of Northeast China and its implications to mantle dynamics. J. Asian Earth Sci. 171, 334-347.

Duan, Y., Zhang, X., Liu, Z., Fang, S., Wang, F., Xu, C., Yuan, Q., 2005. Study on upper mantal discontinuities using the receiver function in the Changbaishan-Jingpohu volcanic area. Chinese J. Geophys. (in Chinese) 48(4), 834-842.

Duan, Y., Zhao, D., Zhang, X., Xia, S., Liu, Z., Wang, F., Li, L., 2009. Seismic structure and origin of active intraplate volcanoes in Northeast Asia. Tectonophysics 470, 257-266.

Fan, Q., Hooper, P., 1991. The Cenozoic basaltic rocks of eastern China: Petrology and chemical composition. J. Petrol. 32, 765-810.

Fan, Q., Sun, J., Liu, R., 2001. Sr-Nd isotopic geochemistry and magmatic evolutions of Wudalianchi volcano, Tianchi volcano and Tengchong volcano. Acta Petrologicaet Mineralogica 20(3), 233-238.

Fan, Q., Zhao, Y., Li, D., Wu, Y., Sui, J., Zheng, D., 2011. Studies on Quaternary volcanism stages of Halaha river and Chaoer river area in the Great Xing'an Range: Evidence from K-Ar dating and volcanic geological features. Acta Petrologica Sinica 27(10), 2827-2832.

Fan, Q., Zhao, Y., Sui, J., Li, D., Wu, Y., 2012. Studies on Quaternary volcanism stages of Nuomin river area in the Great Xing'an Range: Evidence from petrology, K-Ar dating and volcanic geology features. Acta Petrologica Sinica 28(4) 1092-1098.

Gilligan, A., Priestley, K., Roecker, S., Levin, V., Rai, S., 2015. The crustal structure of the western Himalayas and Tibet. J. Geophys. Res.: Solid Earth 120, 3946-3964.

Guo, L., Meng, X., Shi, L., Chen, Z., 2012. Preferential filtering method and its application to Bouguer gravity anomaly of Chinese continent. Chinese J. Geophys. (in Chinese) 55 (12), 4078-4088.

Guo, Z., Cao, Y., Wang, X., Chen, Y., Ning, J., He, W., Tang, Y., Feng, Y., 2014. Crust and upper mantle structures beneath Northeast China from receiver function studies. Earthq. Sci. 27(3), 265-275.

Guo, Z., Chen, Y., Ning, J., Yang, Y., Afonso, J., Tang, Y., 2016. Seismic evidence of ongoing sublithosphere upper mantle convection for intra-plate volcanism in Northeast China. Earth Planet. Sci. Lett. 433, 31-43.

Guo, Z., Wang, K., Yang, Y., Tang, Y., Chen, Y., Hung, S., 2018. The origin and mantle dynamics of quaternary intraplate volcanism in Northeast China from joint inversion of surface wave and body wave. J. Geophys. Res.: Solid Earth 123, 2410-2425.

Hao, T., Liu,. Y., Duan, C., 1997. The eharacteristic of geophysical field in the east China and adjacent regions and its tectonics significance. Chinese J. Geophys. (in Chinese) 40(5), 677-690.

He, P., Lei, J., Yuan, X., Xu, X., Xu, Q., Liu, Z., Mi, Q., Zhou, L., 2018. Lateral Moho variations and the geometry of the Main Himalayan Thrust beneath the Nepal Himalayan orogen revealed by teleseismic receiver functions. Geophys. J. Int. 214, 1004-1017.

He, R., Shang, X., Yu, C., Zhang, H., van der Hilst, R., 2014. A unified map of moho depth and vp/vs ratio of continental china by receiver function analysis. Geophys. J. Int. 199(3), 1910-1918.

Hetland, E., Wu, F., Song, J., 2004. Crustal structure in the Changbaishan volcanic area, China, determined by modeling receiver functions. Tectonophysics 386(3-4), 157-175.

Huang, J., Zhao, D., 2006. High-resolution mantle tomography of China and surrounding regions. J. Geophys. Res.: Solid Earth 111(B9), B09305, doi:10.1029/2005JB004066.

Huang, Z., Li, H., Xu, Y., 2014. Lithopsheric S-wave velocity structure of west China and neighboring areas from surface wave tomography. Chinese J. Geophys. (in Chinese) 57(12), 3994-4004.

Inoue, T., Tanimoto, Y., Irifune, T., Suzuki, T., Fukui, H., Ohtaka, O., 2004. Thermal expansion of wadsleyite, ringwoodite, hydrous wadsleyite and hydrous ringwoodite. Phys. Earth Planet. Inter. 143-144, 279-290.

Kennett, B., Engdahl, R., 1991. Travel times for global earthquake location and phase identification. Geophys. J. Int. 105, 429-465.

Kind, R., et al., 2002. Seismic images of crust and upper mantle beneath Tibet: evidence for Eurasian plate subduction. Science 298, 1219-1221.

Kosarev, G., Kind, R., Sobolev, S., Yuan, X., Hanka, W., Oreshin, S., 1999. Seismic evidence for a detached Indian lithospheric mantle beneath Tibet. Science 283, 1306-1309.

Lei, J., Zhao, D., 2005. P-wave tomography and origin of the Changbai intraplate volcano in Northeast Asia. Tectonophysics 397(3), 281-295.

Lei, J., Zhao, D., 2006. Global P-wave tomography: on the effect of various mantle and core phases. Phys. Earth Planet. Inter. 154(1), 44-69.

Lei, J., Zhao, D., Su,Y., 2009. Insight into the origin of the Tengchong intraplate volcano and seismotectonics in southwest China from local and teleseismic data. J. Geophys. Res. Solid Earth 114, B05302, doi: 10.1029/2008JB005881.

Lei, J., Xie, F., Fan, Q., Santosh, M., 2013. Seismic imaging of the deep structure under the Chinese volcanoes: An overview. Phys. Earth Planet. Inter. 224, 104-123.

Lei, J., Zhao, D., 2016. Teleseismic P-wave tomography and mantle dynamics beneath Eastern Tibet. Geochem. Geophys. Geosyst. 17, 1861-1884.

Lei, J., Zhao, D., Xu, Y., Fan, Q., Mi, Q., Du, M., Lu, M., 2018. Is there a gap in the stagnant Pacific slab in the mantle transition zone under the Changbaishan volcano? Acta Petrologica Sinica 34(1), 13-22.

Lei, J., Zhao, D., Xu, X., Xu, Y., Du, M., 2019. Is there a big mantle wedge structure under eastern Tibet? Phys. Earth Planet. Inter. 292, 100-113.

Lei, J., Zhao, D., Xu, X., Du, M., Mi, Q., Lu, M., 2020. P-wave upper-mantle tomography of the Tanlu fault zone in eastern China. Phys. Earth Planet. Inter. 299, 106402.

Li, S., Mooney, W., Fan, J., 2006. Crustal structure of mainland China from deep seismic sounding data. Tectonophysics 420, 239-252.

Li, X., Yuan, X., 2003. Receiver functions in northeast China--implications for slab pentration into the lower mantle in northwest Pacific subduction zone. Earth Planet. Sci. Lett. 216, 679-691.

Li Y., Gao M., Wu Q., 2014. Crustal thickness map of the chinese mainland from teleseismic receiver functions. Tectonophysics 611, 51-60.

Liang, C., Song, X., Huang, J., 2004. Tomographic inversion of Pn travel times in China. J. Geophys. Res.: Solid Earth 109, B11304, doi: 10.1029/2003JB002789.

Liu, H., Niu, F., 2011. Receiver function study of the crustal structure of Northeast China: seismic evidence for a mantle upwelling beneath the eastern flank of the Songliao Basin and the Changbaishan region. Earthq. Sci. 24(1), 27-33.

Liu, J., 1999. Chinese volcanoes. Science Press, Beijing, pp. 5-8.

Liu, R., 2000. Active volcanoes in China. Seismological Press, Beijing, pp. 11-44.

Lu, M., Lei, J., Zhang, G., 2019. Upper-mantle seismic anisotropy structure and dynamics beneath NE China inferred from SKS splitting analysis. Chinese J. Geophys. (in Chinese) 62(9), 3365-3384.

Lu, Z., Xia, H., 1993. Geoscience transect from Dong Ujimqinqi, Nei Mongol, to Donggoum Liaoning, China. Chinese J. Geophys. (in Chinese) 36(6), 765-772.

Ma, J., Tian, Y., Liu, C., Zhao, D., Feng, X., Zhu, H., 2018. P-wave tomography of Northeast Asia: Constraints on the western Pacific plate subduction and mantle dynamics. Phys. Earth Planet. Inter. 274, 105-126.

Mavko, G., 1980. Velocity and attenuation in partially molten rocks. J. Geophys. Res. 85(B10), 5173-5189.

Meng, Q., 2003. What drove late Mesozoic extension of the northern China–Mongolia tract? Tectonophysics 369, 155-174.

Meng, E., Xu, W., Pei, F., Yang, D., Yu, Y., Zhang, X., 2010. Detrital-zircon geochronology of Late Paleozoic sedimentary rocks in eastern Heilongjiang Province, NE China: Implications for the tectonic evolution of the eastern segment of the Central Asian Orogenic Belt. Tectonophysics 485, 42-51.

Meng, E., Xu, W., Pei, F., Yang, D., Wang, F., Zhang, X., 2011. Permian bimodal volcanism in the Zhangguangcai range of eastern Heilongjiang Province, NE China: Zircon U-Pb-Hf isotopes and geochemical evidence. J. Asian Earth Sci. 41, 119-132.

O'Connell, R., Budiansky, B., 1974. Seismic velocities in dry and saturated cracked solid. J. Geophys. Res. 79(35), 5412-5426.

Pan, J., Li, Y., Wu, Q., Yu, D., 2014. 3-D S-wave velocity structure of crust and uppermantle beneath the northeast China. Chinese J. Geophys. (in Chinese) 57 (7), 2077-2087.

Qiu, G., Pei, F., Feng, H., Du, B., Zhang, X., Zhang, P., Yuan, Y., He, M., Bai, D., 2014. Analysis of magma chamber at the Tianchi volcano area in Changbai Mountain. Chinese J. Geophys. (in Chinese) 57(10), 3466-3477.

Ren, J., Tamaki, K., Li, S., Zhang, J., 2002. Late Mesozoic and Cenozoic rifting and its dynamic setting in eastern China and adjacent areas. Tectonophysics 344, 175-205.

Sengör, A., Natal'In, B., Burtman, V., 1993. Evolution of the Altaid tectonic collage and Paleozoic crustal growth in Eurasia. Nature 364, 299-307.

Staudigel, H, King, S., 1992. Ultrafast subduction: the key to slab recycling efficiency and mantle differentiation? Earth Planet. Sci. Lett. 109, 517-530.

Su, B., Qin, K., Tang, D., Sakyi, P., Liu, P., Sun, H., Xiao, Q., 2013. Late Paleozoic mafic–ultramafic intrusions in southern Central Asian Orogenic Belt (NW China): Insight into magmatic Ni-Cu sulfide mineralization in orogenic setting. Ore Geol. Rev. 51:57-73.

Tang, J., Liu, T., Liu, D., Zhao, G., Wang, J., Zhan, Y., 1997. Preliminary observations of the Tianchi volcano area in Changbaishan mountain by MT method. Seismol. Geol. 19(2), 164-170.

Tang, Y., Xu, W., Wang, F., Wang, W., Xu, M., Zhang, Y., 2014. Geochronology and geochemistry of Early-Middle Triassic magmatism in the Erguna Massif, NE China: Constraints on the tectonic evolution of the Mongol-Okhotsk Ocean. Lithos 184, 1-16.

Tatsumi, Y., Maruyama, S., Nohda, S., 1990. Mechanism of backarc opening in the Japan Sea: role of asthenospheric injection. Tectonophysics 181, 299-306.

Tao, K., Niu, F., Ning, J., Chen, Y., Grand, S., Kawakatsu, H., Tanaka, S., Obayashi, M., Ni, J., 2014. Crustal structure beneath NE China imaged by NECESSArray receiver function data. Earth Planet. Sci. Lett. 398, 48-57.

Thompsons, A., 1992. Water in the Earth’s upper mantle. Nature 358, 295-302.

Tian, Y., Zhu, H., Zhao, D., Liu, C., Feng, X., Liu, T., Ma, J., 2016. Mantle transition zone structure beneath the Changbai volcano: Insight into deep slab dehydration and hot upwelling near the 410 km discontinuity. J. Geophys. Res.: Solid Earth 121, 5794-5808.

Wei, W., Xu, J., Zhao, D., Shi, Y., 2012. East Asia mantle tomography: New insight into plate subduction and intraplate volcanism. J. Asian Earth Sci. 60, 88103.

Wei, W., Zhao, D., Xu, J., Wei, F., Liu, G., 2015. P and S wave tomography and anisotropy in Northwest Pacific and East Asia: Constraints on stagnant slab and intraplate volcanism. J. Geophys. Res.: Solid Earth 120, 1642-1666.

Wei, Z., Chen L., 2012. Regional differences in crustal structure beneath northeastern China and northern North China Craton: constraints from crustal thickness and Vp/Vs ratio. Chinese J. Geophys. (in Chinese) 55(11), 3601-3614.

Wessel P., Smith W., 1995. New, improved version of generic mapping tools released. Eos Transactions, 79, 47-47.

Wu, F., Sun, D., Jahn, B., Wilde, S., 2004. A Jurassic garnet-bearing granitic pluton from NE China showing tetrad REE patterns. J. Asian Earth Sci. 23, 731-744.

Wu, F., Zhao, G., Sun, D., Wilde, S., Yang, J., 2007. The Hulan Group: its role in the evolution of the Central Asian Orogenic Belt of NE China. J. Asian Earth Sci. 30, 542-556.

Xiong, X., Gao, R., Hou, H., Li, W., Li, H., Liu, C., 2016. Deep structure geometry features of Nenjing fault zone and crustal deformation revealed by deep seismic reflection profile. Chinese J. Geol. (in Chinese) 51(3), 694-705.

Xu, W., Ji, W., Pei, F., Meng, E., Yu, Y., Yang, Z., Zhang, X., 2009. Triassic volcanism in eastern Heilongjiang and Jilin provinces, NE China: Chronology, geochemistry, and tectonic implications. J. Asian Earth Sci. 34(3), 392-402.

Xu, W., Pei, F., Wang, F., Wang, W., 2013. Spatial-temporal relationships of Mesozoic volcanic rocks in NE China: Contraints on tectonic overprinting and transformations between multiple tectonic regimes. J. Asian Earth Sci. 74, 167-193.

Yang, B., Mu, S., Jin, X., Liu, C., 1996. Synthesized study on the Geophysics of Manzhouli-Suifenhe Geoscience Transect, China. Chinese J. Geophys. (in Chinese) 39(6), 772-782.

Yang, G., Xue, L., Liu, Z., Liu, J., 2001. Studies of deep geology with seismic section interpretation in Songliao basin. Oil Gas Geol. 22(4), 326-336.

Yang, Y., Lei, J., Ai, Y., Zhang, G., Sun, C., Fan, E., Li, L., Mi, Q., Lu, M., He, J., Wang, J., Du, M., Zhang, B., Tian, F., Ma, C., Liu, Z., 2019a. Crustal structure beneath Northeast China from ambient noise tomography. Phys. Earth Planet. Inter. 293, 106257.

Yang, Y., Lei, J., Zhang, G., Liang, X., Sun, C., Mi, Q., Lu, M., Du, M., Zhang, B., Tian, F., He, J., Wang, J., Wu, B., Ma, C., Liu, Z., 2019b. Crustal velocity structure and seismogenic environment in the source areas of the Qianguo Ms

5.8 and Songyuan Ms 5.7 earthquakes. Chinese J. Geophys. (in Chinese) 62(11), 4259-4278.

Yin, W., Lei, J., Du, M., Yang, Y., Mi, Q., Lu, M., Lin, F., 2019. Uppermost-mantle Pn velocity and anisotropic tomography of the Tanlu fault zone and adjacent areas. Chinese J. Geophys. (in Chinese) 62(11), 4227-4238.

Yuan, X., Ni, J., Kind, R., Mechie, J., Sandvol, E., 1997. Lithospheric and upper mantle structure of southern Tibet from a seismological passive source experiment. J. Geophys. Res.: Solid Earth 102, 27491–27500.

Yuan, X., Sobolev, S., Kind, R., 2002. Moho topography in the Central Andes and its geodynamic implications, Earth Planet. Sci. Lett. 199(3-4), 389-402.

Zhang, C., Zhang, X., Zhao, J., Liu, B., Zhang, J., Yang, Z., Hai, Y., Sun, G., 2002. Crust–mantle structure of the Changbaishan Tianchi volcanic region and its vicinity: an exploratory study and inferences. Chinese J. Geophys. (in Chinese) 45(6), 862-871.

Zhang, G., Lei, J., Sun, D., 2019a. The 2013 and 2017 Ms 5 seismic swarms in Jilin, NE China: Fluid-triggered earthquakes? J. Geophys. Res.: Solid Earth 124, 13096-13111.

Zhang, G., Wu, Q., Pan, J., Zhang, F., Yu, D., 2013. Study of crustal structure and Poisson ratio of NE China by H-κ stack and CCP stack methods. Chinese J. Geophys. (in Chinese) 56(12), 4084-4094.

Zhang, J., Gao, S., Ge, W., Wu, F., Yang, J., Wilde, S., Li, M., 2010. Geochronology of the Mesozoic volcanic rocks in the Great Xing'an Range, northeastern China: Implications for subduction-induced delamination. Chem. Geol. 276(3-4), 144-165.

Zhang, R., Wu, Q., Sun, L., He, J., Gao, Z., 2014. Crustal and lithospheric structure of Northeast China from S-wave receiver functions. Earth Planet. Sci. Lett. 401, 196-205.

Zhang, P., Yao, H., Chen, L., Fang, L., Wu, Y., Feng, J., 2019b. Moho depth variations from receiver function imaging in the northeastern North China Craton and its tectonic implications. J. Geophys. Res.: Solid Earth 124, 1852-1870.

Zhang, X., Yang, B., Wu, F., Liu, G., 2006. The lithosphere structure in the Hingmong Jihei (Hinggan Mongolia-JilinHeilongjiang) region, northeastern China. Geol. China (in Chinese) 33(4), 816-823.

Zhao, D., 2004. Global tomographic images of mantle plumes and subducting slabs: insight into deep Earth dynamics. Phys. Earth Planet. Inter., 146, 3-34.

Zhao, D., Maruyama, S., Omori, S., 2007. Mantle dynamics of Western Pacific and East Asia: Insight from seismic tomography and mineral physics. Gondwana Res. 11, 120-131.

Zhao, D., Tian, Y., Lei, J., Liu, L., Zheng, S., 2009. Seismic image and origin of the Changbai intraplate volcano in East Asia: Role of big mantle wedge above the stagnant Pacific slab. Phys. Earth Planet. Inter. 173, 197-206.

Zhao, D., Tian, Y., 2013. Changbai intraplate volcanism and deep earthquakes in East Asia: a possible link? Geophys. J. Int. 195, 706-724.

Zheng, X., Yao, Z., Liang, J., Zheng, J., 2010. The role played and opportunity provided by IGP DMC of China National Seismic Network in Wenchuan Earthquake Disaster Relief and Researches. Bull. Seismol. Soc. Am. 100, 2866-2872.

Zhu, H., Tian, Y., Liu, C., Feng, X., Yang, B., Liu, C., Liu, Y., Ma, J., 2017. High-resolution crustal structure of Northeast China revealed by teleseismic receiver functions. Chinese J. Geophy. (in Chinese) 60(5), 1676-1689.

Figure Captions

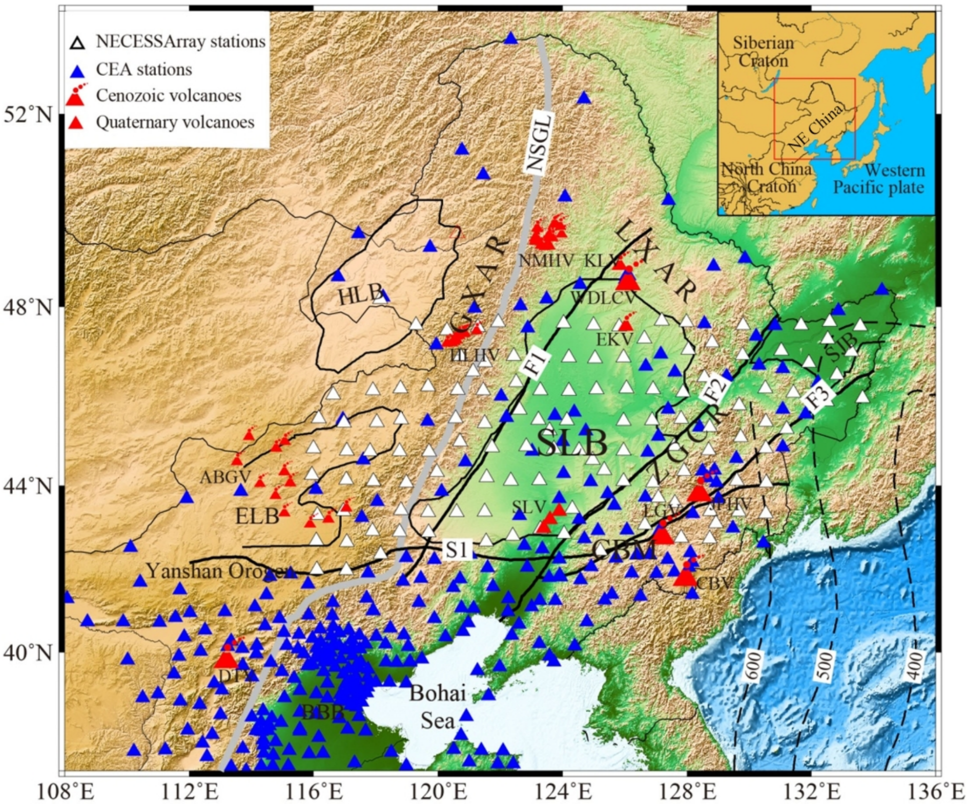

Fig. 1. Sketch map showing the major tectonic units and CEA (blue triangles) and NECESSArray (white triangles) seismic stations used in this study. Red triangles with and without smoking represent Cenozoic and Quaternary volcanoes, respectively. Thin solid lines are boundaries of the basins, whereas thick solid lines denote major active faults in the region (Deng et al., 2002). The black dashed lines with numbers represent the upper boundary depth of the subducting Pacific slab, whereas the thick gray line denotes the North-South Gravity Lineament (NSGL). GXAR, the Great Xing'an range; LXAR, the Lesser Xing'an range; ZGCR, the Zhangguangcai range; CBM, the Changbaishan mountain. SLB, the Songliao basin; HLB, the Hailar basin; ELB, the Erlian basin; SJB, the Sanjiang basin; BBB, the Bohai Bay basin. CBV, the Changbaishan volcano; JPHV, the Jingpohu volcano; LGV, the Longgang volcano. WDLCV, the Wudalianchi volcano; KLV, the Keluo volcano; EKV, the Erke volcano. SLV, the Shuangliao volcano. DTV, the Datong volcano. NMHV, the Nuominhe volcanic group; HLHV, the Halaha volcanic group; ABGV, the Abaga volcanic group. F1, the Nenjiang-Balihan fault; F2, the Yilan-Yitong fault; F3, the Dunhua-Mishan fault; S1, the Solonker suture. The upper-right inset shows the location of the study area.

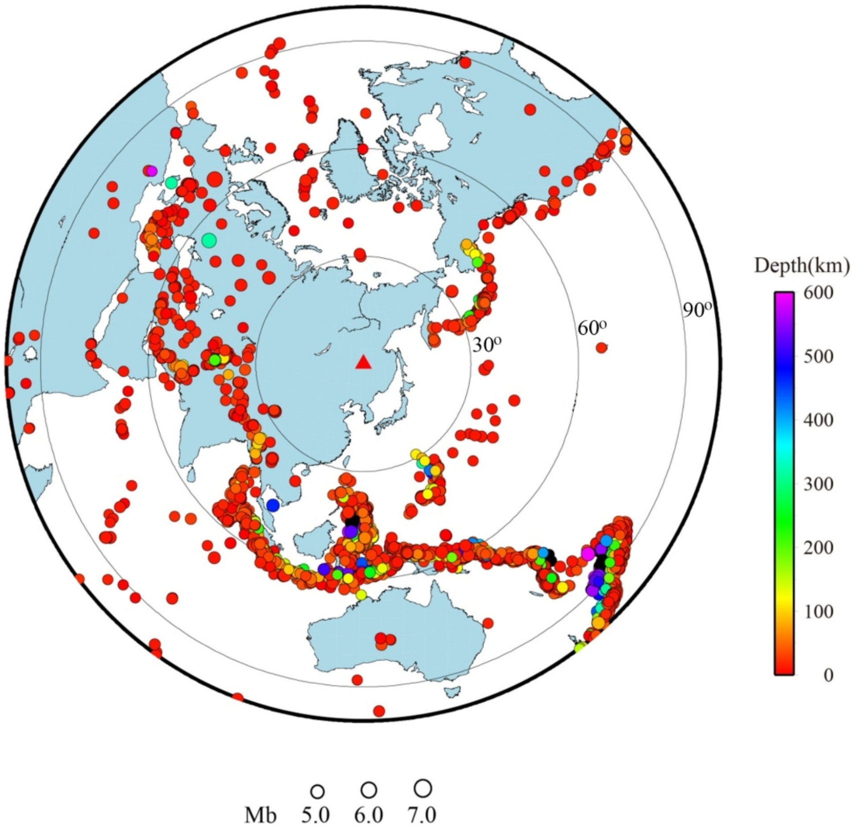

Fig. 2. Distribution of the 2903 teleseismic events (dots) used in the P wave receiver function analyses. Red and blue colors denote shallower and deeper events, respectively, the color scale of which is shown on the right. Magnitude scale of events is shown at the bottom. The big circles with the numbers in degrees denote the distances from the center of the study region (the red triangle).

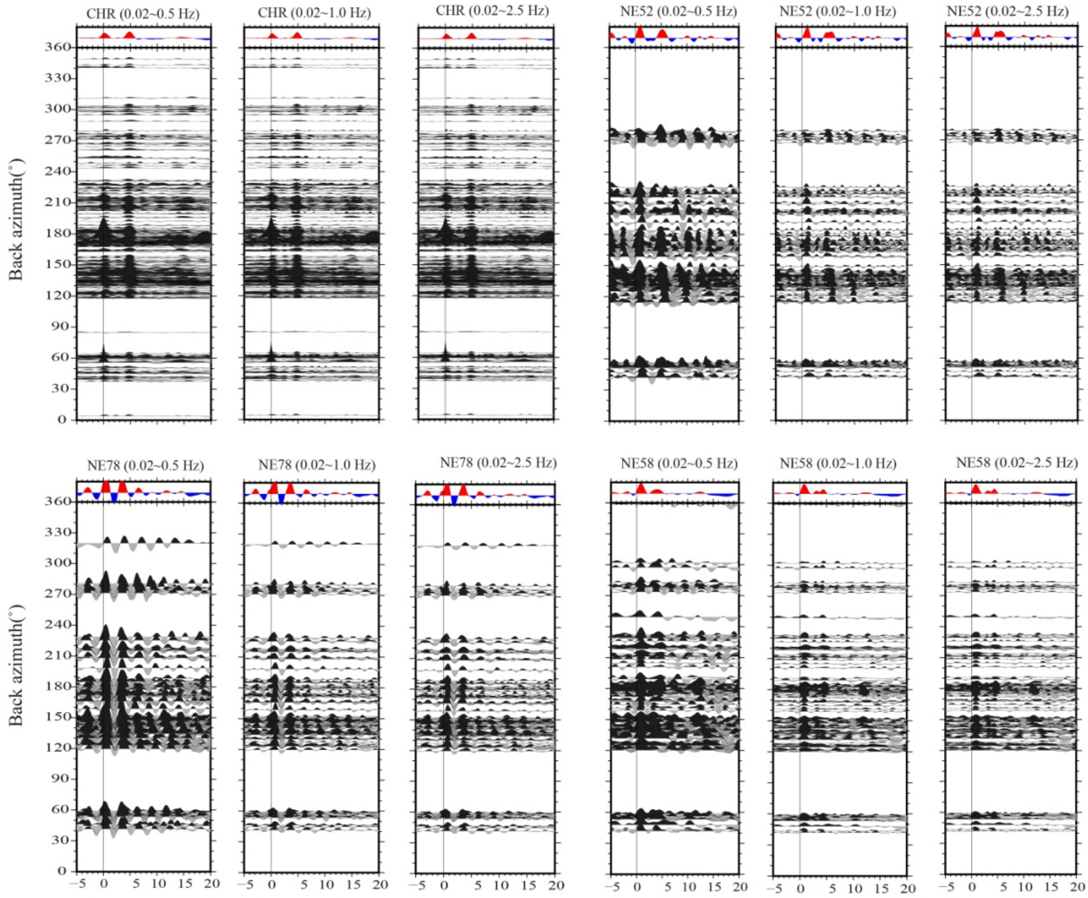
CHR (0.02~0.5 Hz)
CHR (0.02~1.0 Hz)
CHR (0.02~2.5 Hz)
NE52 (0.02~0.5 Hz)
NE52 (0.02~1.0 Hz)
NE52 (0.02~2.5 Hz)
NE78 (0.02~0.5 Hz)
NE78 (0.02~1.0 Hz)
NE78 (0.02~2.5 Hz)
NE58 (0.02~0.5 Hz)
NE58 (0.02~1.0 Hz)
NE58 (0.02~2.5 Hz)
Back azimuth(°)

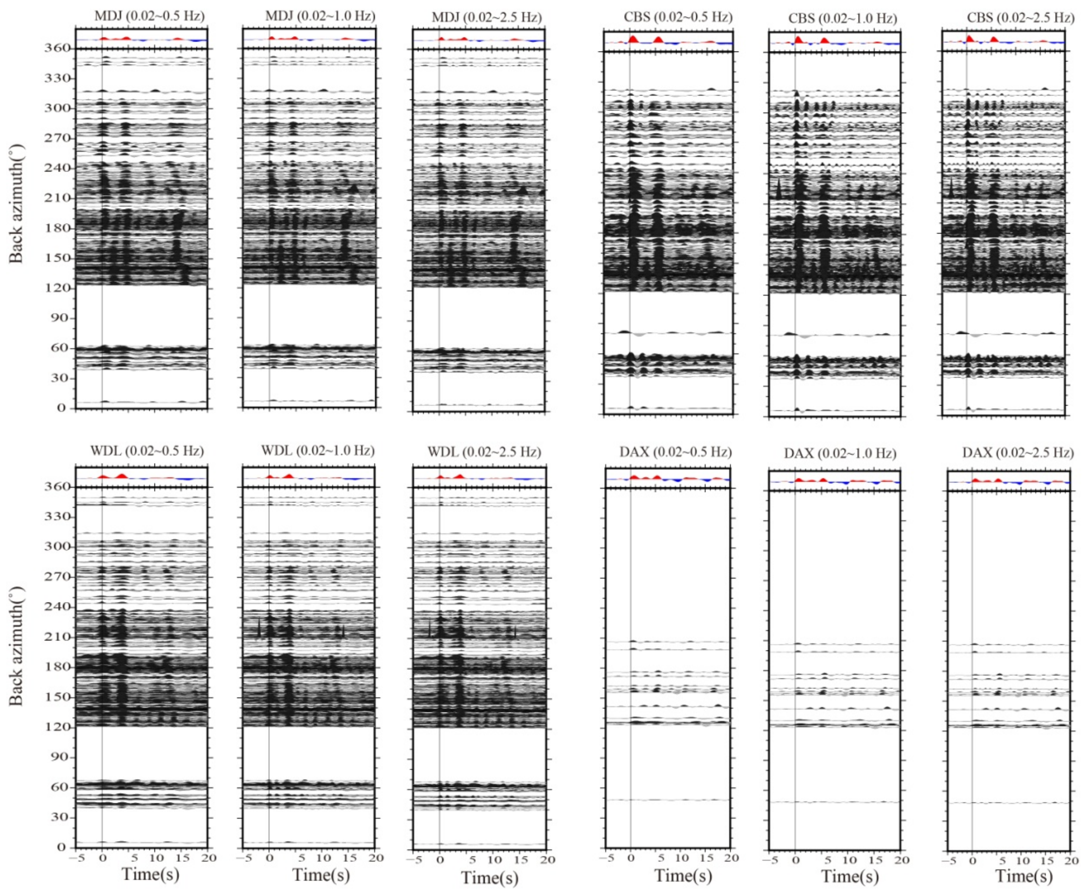
MDJ (0.02~0.5 Hz)
MDJ (0.02~1.0 Hz)
MDJ (0.02~2.5 Hz)
CBS (0.02~0.5 Hz)
CBS (0.02~1.0 Hz)
CBS (0.02~2.5 Hz)
WDL (0.02~0.5 Hz)
WDL (0.02~1.0 Hz)
WDL (0.02~2.5 Hz)
DAX (0.02~0.5 Hz)
DAX (0.02~1.0 Hz)
DAX (0.02~2.5 Hz)
Back azimuth(°)
Time(s)

Fig. 3. Individual receiver functions aligned with the back-azimuth (in degrees) at three frequency bands for eight stations CHR, NE52, NE78, NE58, MDJ, CBS, WDL and DAX. The color plot shows the stacked receiver function from all the back-azimuthal receiver functions recorded at the station. The corresponding station code and frequency band are shown on the top. Locations of these stations are illustrated in black triangles in Fig. 5, and these stations are situated in the northern Great Xing’an range, the southern Great Xing’an range, the western Songliao basin, the eastern Songliao basin, the Zhangguangcai range, the Changbaishan mountain, the Lesser Xing'an rang, and the northeastern North China Craton, respectively. The upper bounds of three frequency bands are set to 0.5, 1.0 and 2.5 Hz, respectively, whereas all the lower bounds are set to 0.02 Hz.

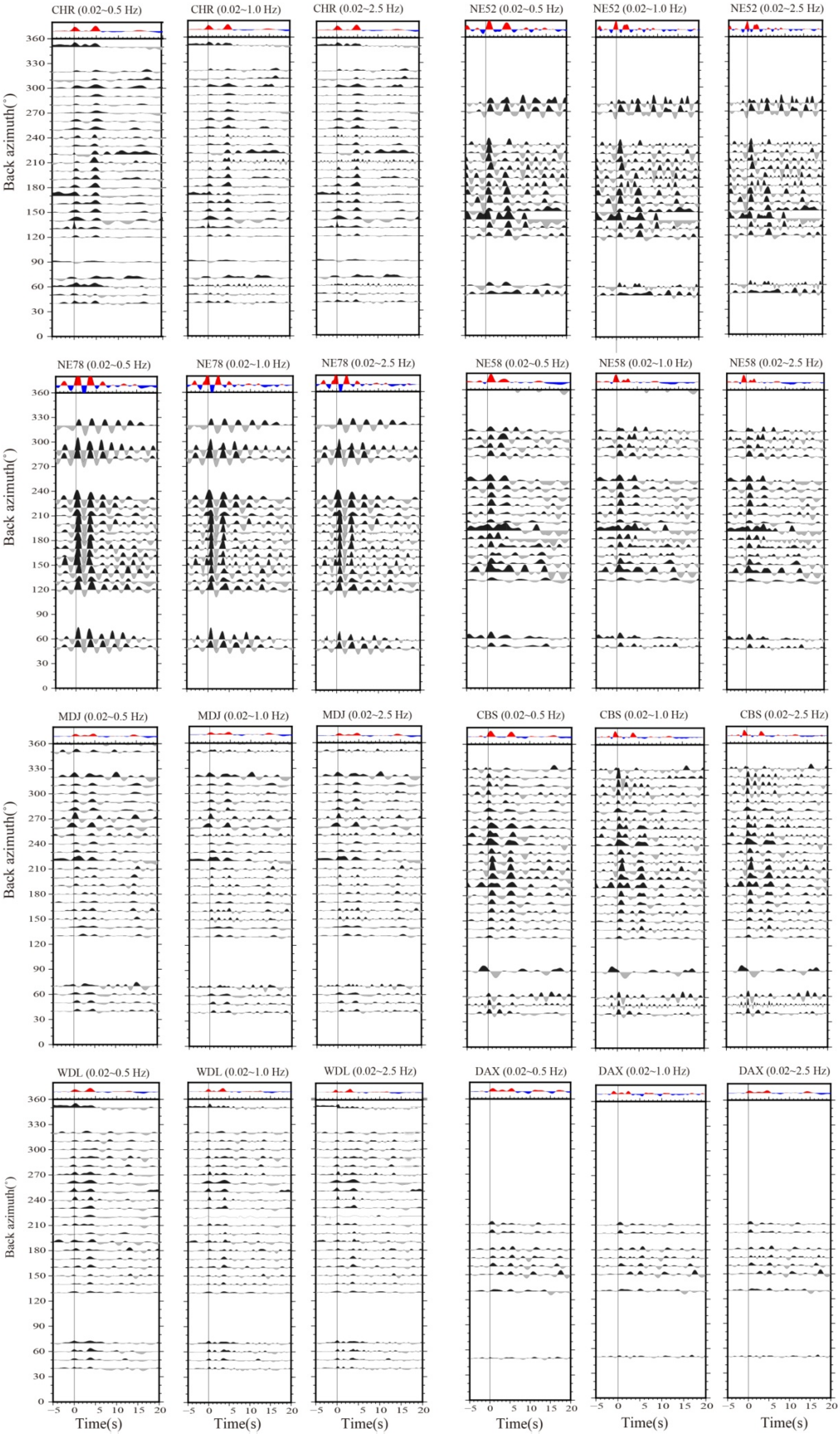

CHR (0.02~0.5 Hz)
CHR (0.02~1.0 Hz)
CHR (0.02~2.5 Hz)
NE52 (0.02~0.5 Hz)
NE52 (0.02~1.0 Hz)
NE52 (0.02~2.5 Hz)
NE78 (0.02~0.5 Hz)
NE78 (0.02~1.0 Hz)
NE78 (0.02~2.5 Hz)
NE58 (0.02~0.5 Hz)
NE58 (0.02~1.0 Hz)
NE58 (0.02~2.5 Hz)
MDJ (0.02~0.5 Hz)
MDJ (0.02~1.0 Hz)
MDJ (0.02~2.5 Hz)
CBS (0.02~0.5 Hz)
CBS (0.02~1.0 Hz)
CBS (0.02~2.5 Hz)
WDL (0.02~0.5 Hz)
WDL (0.02~1.0 Hz)
WDL (0.02~2.5 Hz)
DAX (0.02~0.5 Hz)
DAX (0.02~1.0 Hz)
DAX (0.02~2.5 Hz)
Back azimuth(°)
Time(s)

Fig. 4. The same as Fig. 3 but for move-out corrected and back-azimuthally binning stacked receiver functions. The traces are stacked by a bin of 10° in the back-azimuths.

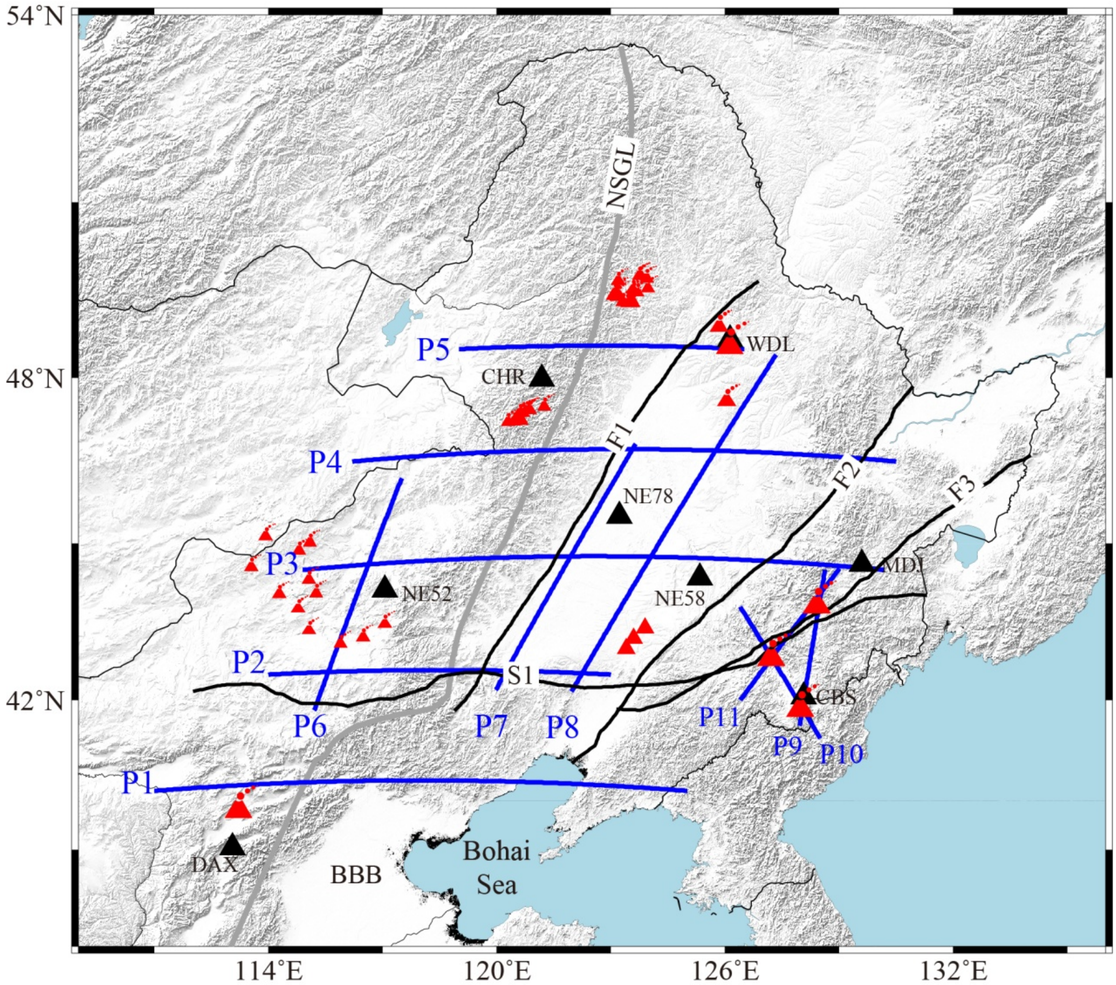

Fig. 5. Distributions of seismic stations (black triangles with station codes) used in Figs. 3 and 4 and receiver function imaging profiles P1-P11 (blue lines) in Figs. 6 and 7. The other labeling is the same as that in Fig. 1.

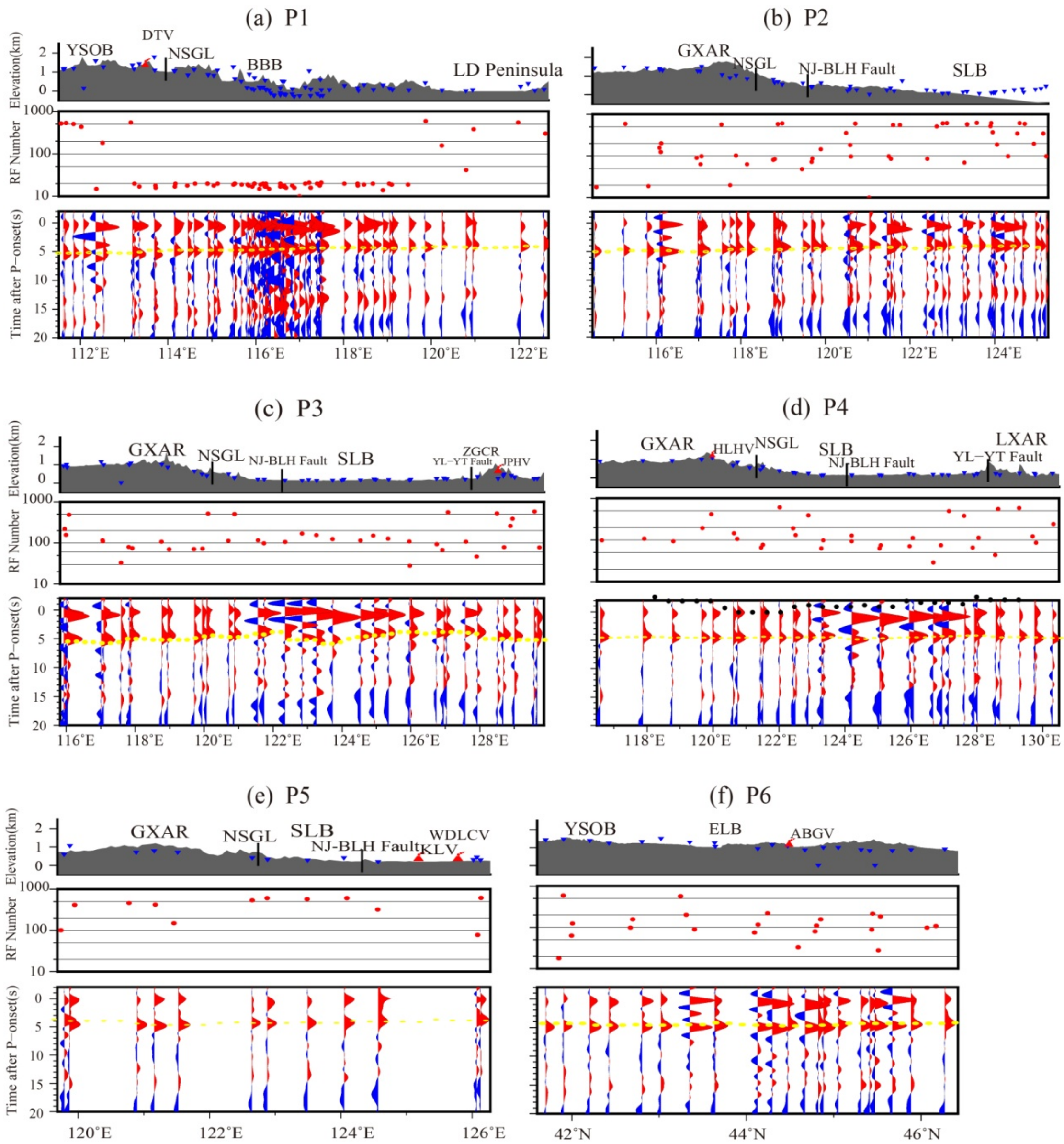

Fig. 6. Binning stacked P receiver functions along profiles P1-P11 as shown in Fig. 5. Surface topography (gray polygons), seismic stations (inverted blue triangles), volcanoes (red triangles), major faults (vertical bars), and main tectonic zones along each profile are plotted on the top. The middle draws the numbers of receiver functions (red dots) used for stacking at each station. The bottom image is the stacked receiver function traces of individual station. **(a-e)** five E-W profiles P1-P5 across different tectonic units; **(f-h)** three NE-SW profiles P6-P8 in the Great Xing'an range and Songliao basin; **(i-k)** three profiles P9-P11 passing through the volcanoes CBV, JPHV and LGV. The Moho conversions connected by yellow dotted lines are shown as the maximum positive Pms amplitudes in a time window of 4-6 s. YSOB, the

Yanshan Orogenic belt; LD peninsula, the Liaodong peninsula; NJ-BLH Fault, the Nenjiang-Balihan Fault; YL-YT Fault, the Yilan-Yitong Fault; SL suture, the Solonker suture. The other labeling is the same as that in Fig. 1.

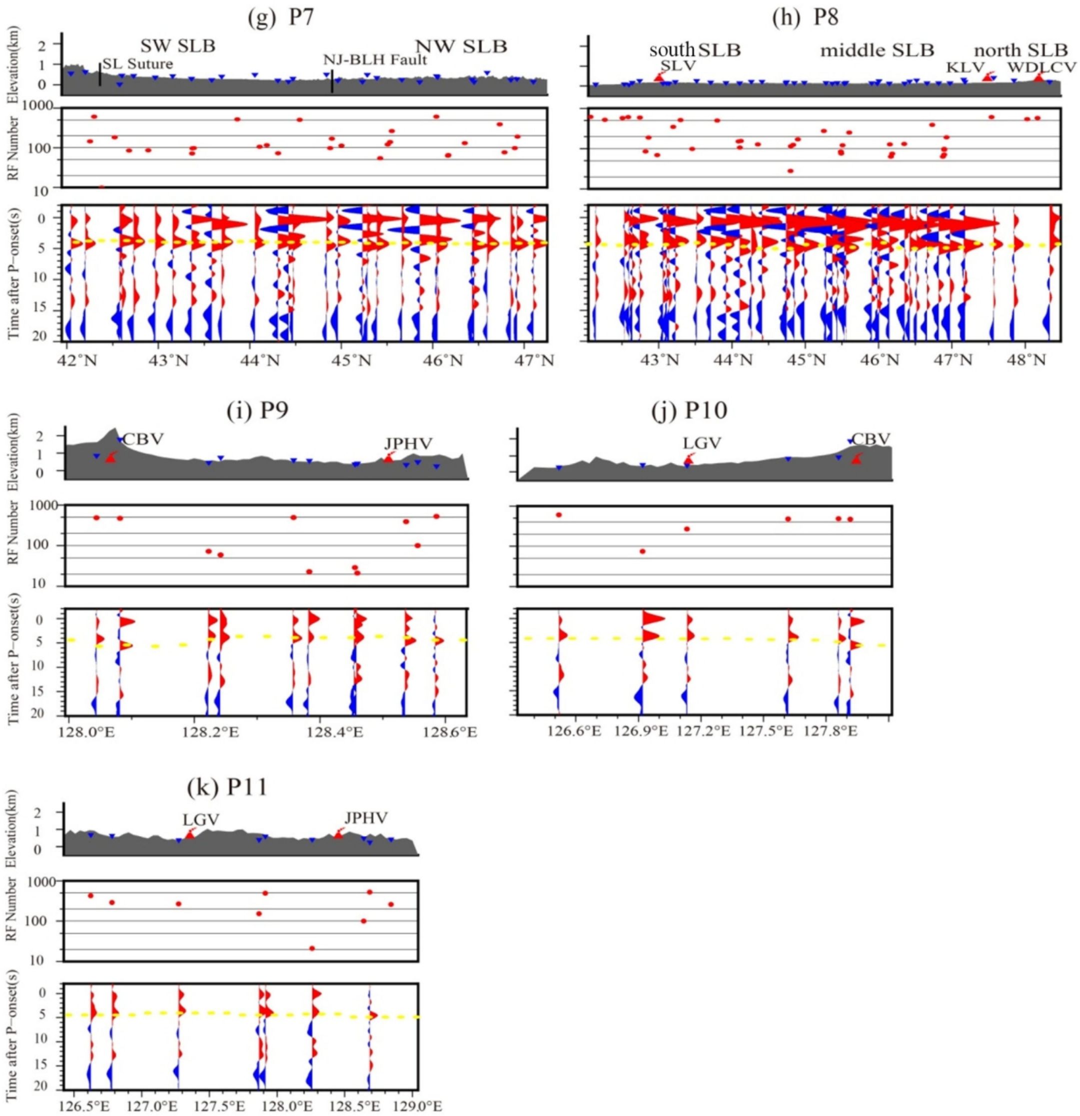

Fig. 6. (Continued).

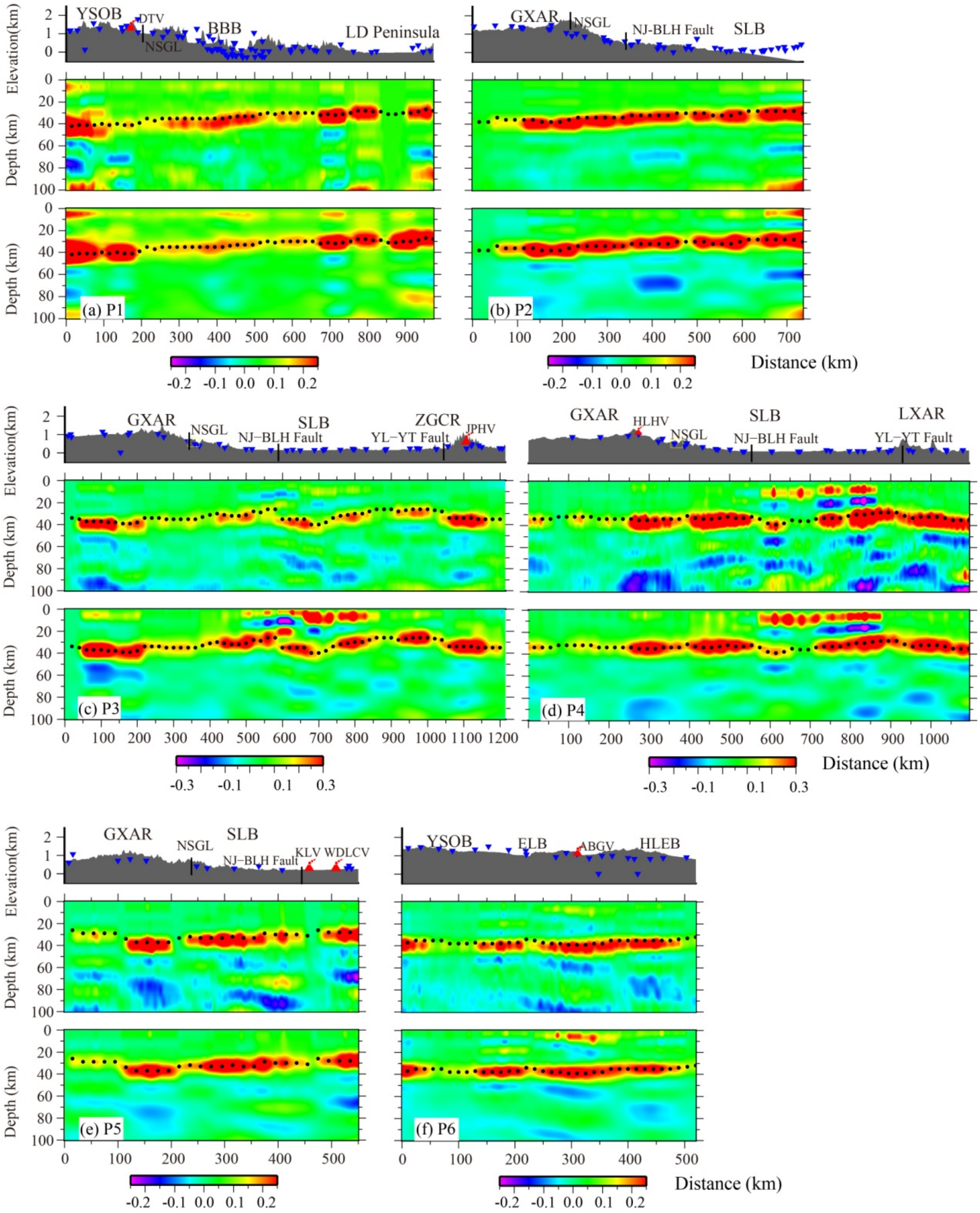

Fig. 7. The same as Fig. 6 but for back-projected (middle) and Fresnel-zone (bottom) migration images in the depth domain along profiles P1-P11 as shown in Fig. 5. Black dots mark the Moho interface. The other labeling is the same as that in Fig. 6.

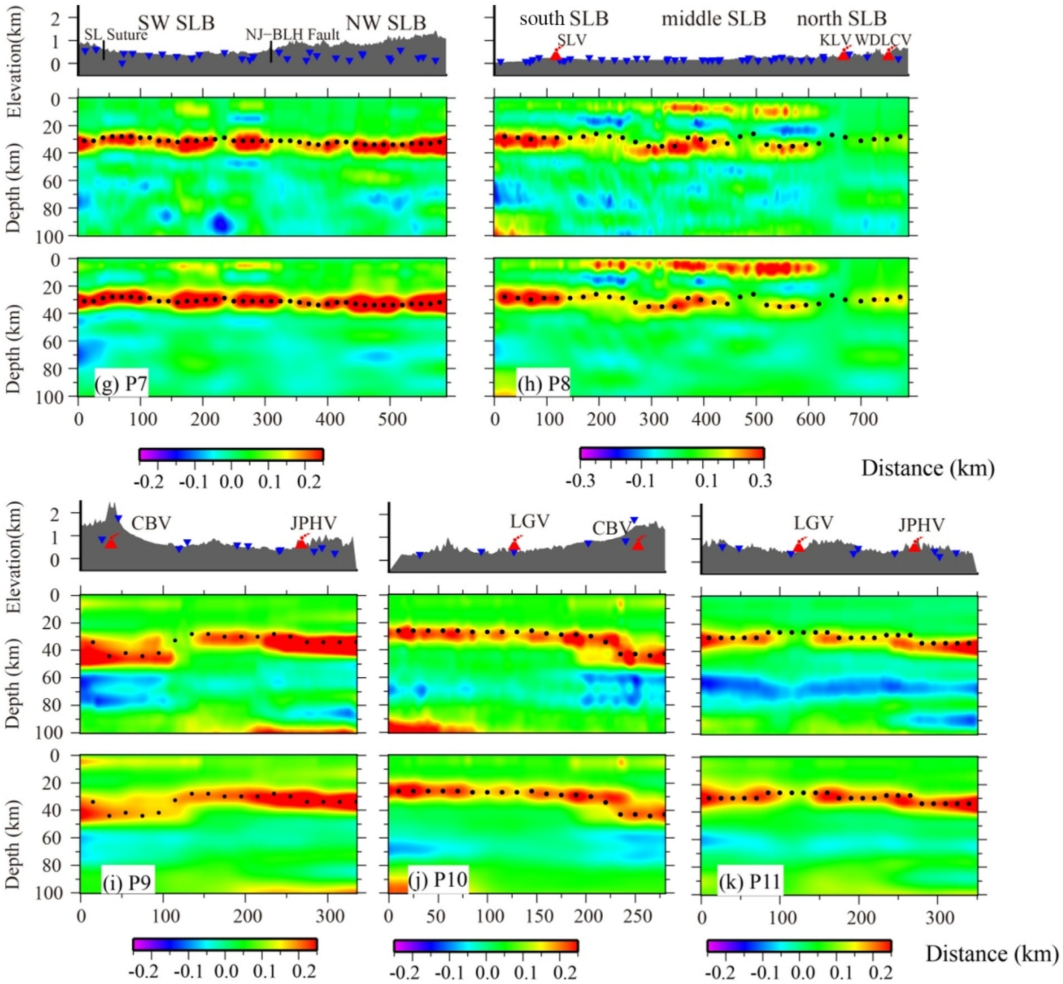

Fig. 7. (Continued).

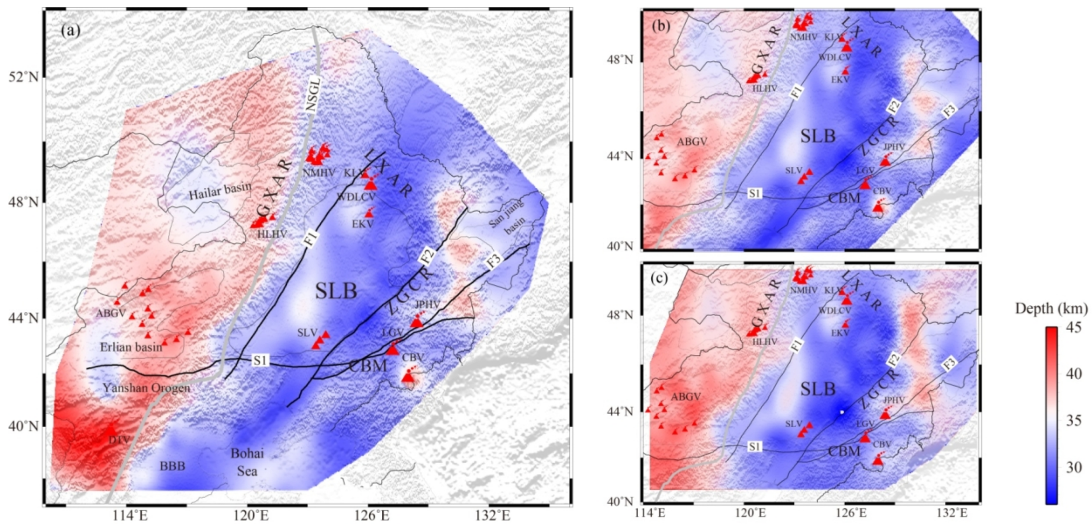

Fig. 8. **(a)** Map of Moho depth derived from receiver function imaging beneath NE China. **(b)** The Moho depth inferred by the present study. **(c)** The same as (b) but from Tao et al. (2014). Red and blue colors show deeper and shallower Moho discontinuity, respectively, the scale of which is shown on the right. The other labeling is the same as that in Fig. 1.

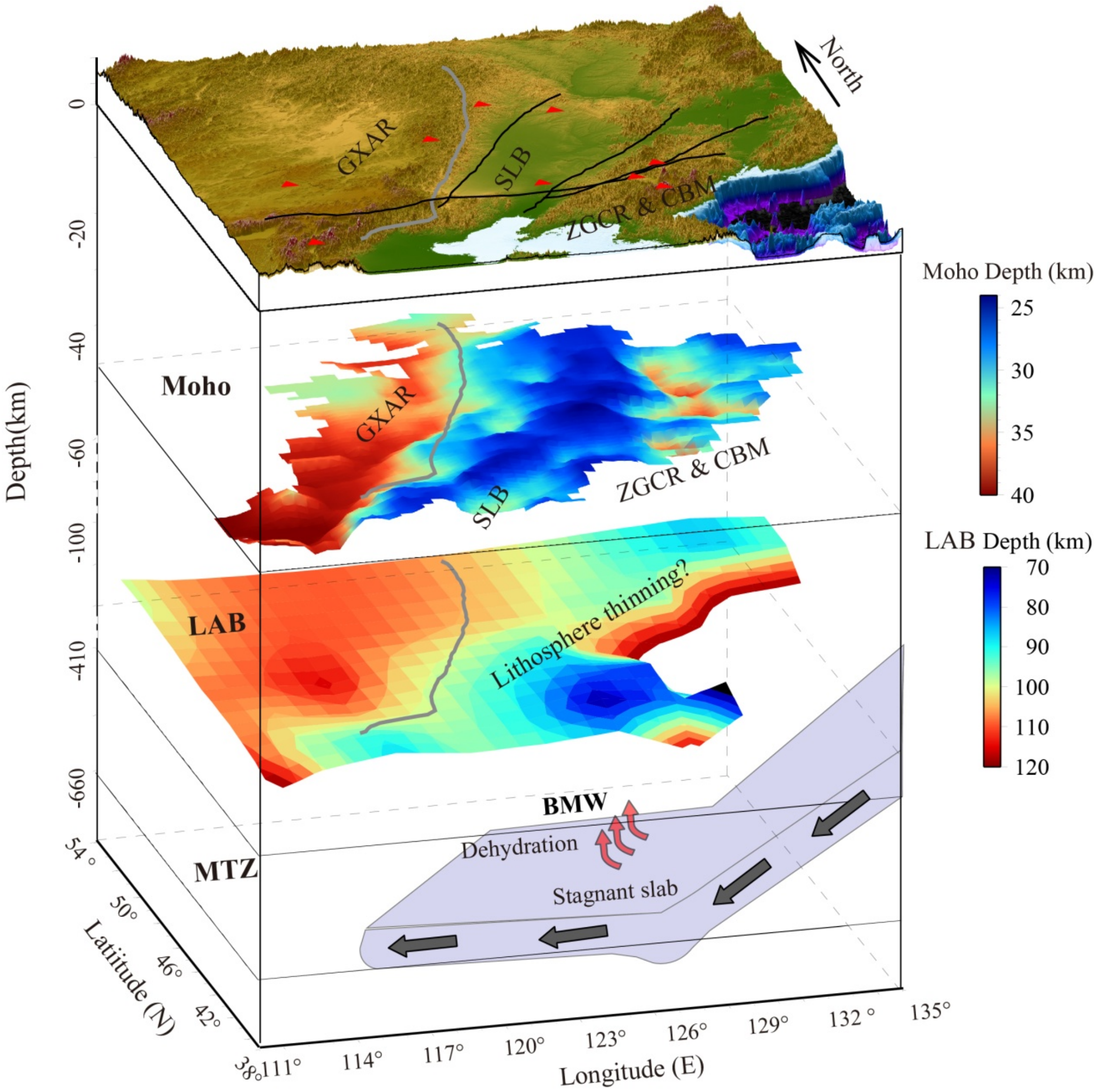

Fig. 9. A possible schematic dynamic model beneath NE China. The topography relief in the study area is shown on the top, in which the gray solid line represents the North-South Gravity Lineament and red triangles symbolize the volcanoes in the study region. The first middle layer exhibits the Moho variations in a 3D perspective view inferred by the present study. Red and blue colors denote deeper and shallower Moho discontinuities, respectively, the scale of which is shown on the right. The second middle indicates the lithosphere-asthenopshere boundary (LAB) depth beneath NE China (An and Shi, 2006). Red and blue colors denote deeper and shallower LAB depths, respectively, the scale of which is shown on the right. At the bottom, a cartoon model contains deep mantle upwelling (red curved arrows) caused by dehydration reactions of the hydrous minerals in the stagnant Pacific slab in the mantle transition

zone (MTZ) and corner flows caused by the subducting Pacific slab (black arrows) in the upper mantle. The upwelling flow feeds the Changbaishan volcanism and causes the lithosphere thinning and the Moho variations in the study region. Such dynamic processes took place in a big mantle wedge (BMW) formed by the deep subduction and long stagnancy of the Pacific slab in the MTZ (e.g., Zhao, 2004; Lei and Zhao, 2005, 2006; Huang and Zhao, 2006; Zhao et al., 2007, 2009; Wei et al., 2012; Zhao and Tian, 2013; Tian et al., 2016; Chen et al., 2017; Lei et al., 2018, 2020; Ma et al., 2018). The other labeling is the same as that in Fig. 1.